Optical limiters based on PT-symmetry breaking of reflectionless modes

Leonardo Salvini¹, Francesco Riboli^{2,3}, Rodion Kononchuk^{4,5}, Federico Tommasi¹, Alice Boschetti^{1,3}, Suwun Suwunnarat⁴, Igor Anisimov⁶, Ilya Vitebskiy⁶, Diederik S. Wiersma^{1,3,7}, Stefano Cavalieri¹, Tsampikos Kottos⁴, and Andrey A. Chabanov⁵

¹Dipartimento di Fisica e Astronomia, Università degli Studi di Firenze, 50019 Sesto Fiorentino, Italy

²Istituto Nazionale di Ottica, Consiglio Nazionale delle Ricerche, 50019 Sesto Fiorentino, Italy
 ³European Laboratory for Nonlinear Spectroscopy (LENS), 50019 Sesto Fiorentino, Italy
 ⁴Department of Physics, Wesleyan University, Middletown, Connecticut 06459, USA
 ⁵Department of Physics and Astronomy, University of Texas at San Antonio, San Antonio, Texas 78249, USA

⁶Sensors Directorate, Air Force Research Laboratory, Wright-Patterson AFB, Ohio 45433, USA

⁷Istituto Nazionale di Ricerca Metrologica, 10125 Torino, Italy

ABSTRACT

We have developed a new method for optical limiting using a system of coupled optical cavities with a PT-symmetric spectrum of reflectionless modes. The optical limiting occurs when the PT symmetry is broken due to the thermo-optic effect in one of the cavities. In our experiment, we used a two-cavity resonator with PT-symmetric spectral degeneracy of reflectionless modes created from alternating layers of cryolite and ZnS. We demonstrated optical limiting by measuring a single 532-nm 6-ns laser pulse. Our experimental results are supported by thermo-optical simulations, which provide deeper insight into the dynamics of the limiting process. Compared to existing limiter designs, our optical limiter offers a customizable limiting threshold, high damage threshold, nanosecond activation time, and broadband laser protection. Additionally, we have shown a method to achieve an even broader transmission spectral bandwidth by implementing this concept in a four-cavity resonator with greater coupling strength using similar materials.

Keywords: Optical limiter, PT-symmetry breaking, Reflectionless modes, Passive optical limiting, Thermoptic effect

1. INTRODUCTION

Optical limiters (OLs) are designed to protect sensitive optical equipment and human eyes from laser-induced damage by restricting the transmitted light whose intensity exceeds a specific threshold, known as the limiting threshold (LT). Usually, passive OLs (i.e., triggered by the light itself) are made from bulky optical materials with negligible linear and strong nonlinear absorption to allow low-intensity light to pass through and absorb high-intensity radiation. However, this approach has two main issues. Firstly, intense absorption can cause the limiter to overheat, leading to irreversible damage. As a result, the LT of the optical limiter may be very close to or even coincide with the damage threshold (DT). Secondly, the required LT, which varies considerably depending on the application, is typically much lower than the LT achievable with limiters that rely solely on nonlinear absorption.

To address these issues, photonic structures incorporating nonlinear optical materials have been considered.^{2–7} Some of these systems work on a different working principle:^{8–10} for intensities above the LT, the structure becomes highly reflective rather than absorbing by suppressing the resonant cavity modes that form within the cavities at low-intensity stimulation.

Further author information: (Send correspondence to Andrey A. Chabanov)

Andrey A. Chabanov: E-mail: andrey.chabanov@utsa.edu

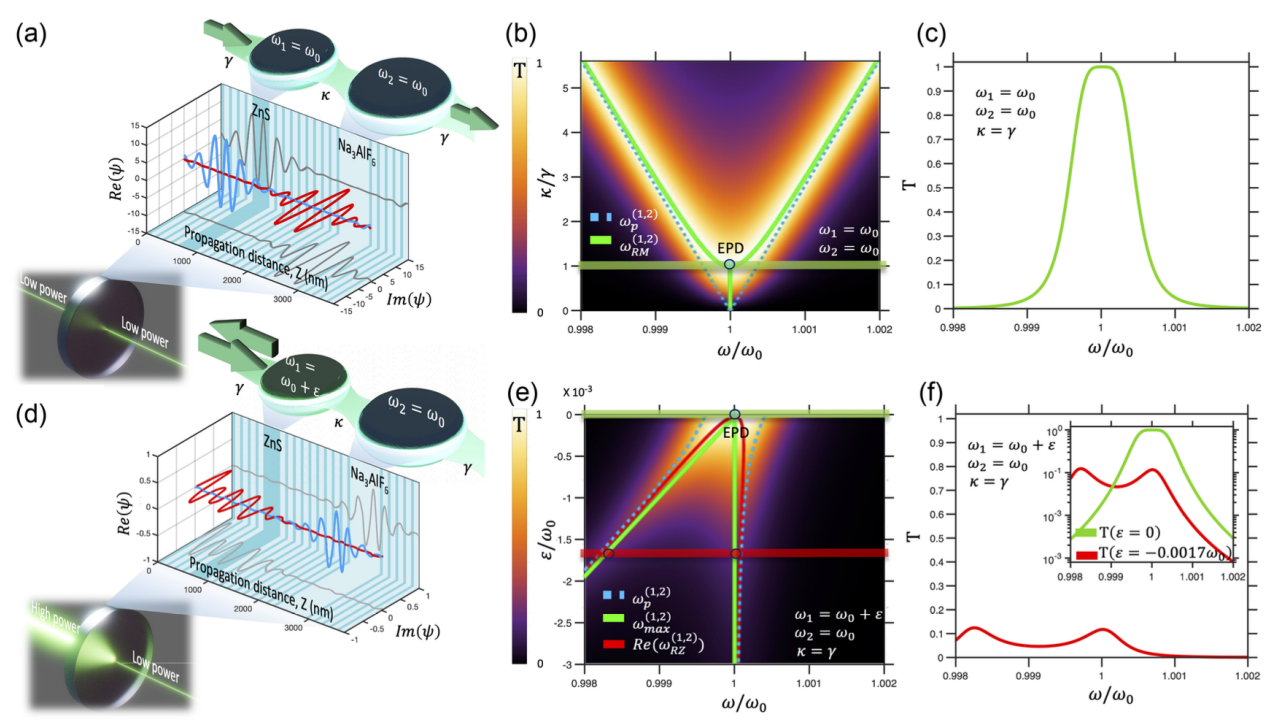


Figure 1. OL based on PT-symmetry breaking of RMs: (a), Artistic view (bottom), schematic (middle), and coupled-mode-theory (CMT) equivalent system (top) of the three-mirror resonator composed of cryolite (Na₃AlF₆) and zinc sulfide (ZnS) layers. The CMT model involves two resonant modes $\omega_1 = \omega_2 = \omega_0$, coupled to each other at rate κ and to respective transmission lines at rates $\gamma_1 = \gamma_2 = \gamma$; (b), (Colormap) transmittance $T(\omega/\omega_0)$ in the parameter space of κ/γ . $\kappa \geq \gamma$ corresponds to the exact PT-symmetry phase, in which the spectrum consists of the complex-conjugate R-zeros $\omega_{RZ}^{(1,2)}$ (vertical green line). At the spontaneous PT-symmetry breaking point, $\kappa = \gamma$, both the frequencies $\omega_{RM}^{(1,2)}$ and the corresponding RSMs $\psi_{RM}^{(1,2)}$ coalesce, forming an EPD at $\omega_{EPD} = \omega_0$ (open circle). The corresponding $\Re(\psi_{EPD})$ and $\Im(\psi_{EPD})$ are shown in (a) by the blue and red lines, respectively. The horizontal green line marks $T_{\kappa=\gamma}(\omega/\omega_0)$, which is plotted in (c). The dashed blue lines indicate the resonance frequencies $\omega_p^{(1,2)}$ (the poles of the S-matrix); (c), Flattop, near-unity transmittance $T_{\kappa=\gamma}(\omega/\omega_0)$ of Eq. 3; (d), Same as (a) but in the case of explicit PT-symmetry breaking due to the mode detuning $\omega_1 = \omega_0 + \varepsilon$, when RSMs no longer exist; (e), (Colormap) transmittance $T_{\kappa=\gamma}(\omega/\omega_0)$ in the parameter space of ε/ω_0 . The dashed blue lines indicate the resonance frequencies $\omega_p^{(1,2)}$. The solid green lines denote the peak transmittance frequencies $\omega_{max}^{(1,2)}$. The solid red lines indicate the real part of the R-zeros, $\Re\{\omega_{RZ}^{(1,2)}\}$. The horizontal red line marks $T_{\kappa=\gamma}(\omega/\omega_0)$ for $\varepsilon/\omega_0 = -0.0017$, which is plotted in (f); (f), Transmittance $T_{\kappa=\gamma}(\omega/\omega_0)$ of Eq. 4 for $\varepsilon/\omega_0 = -0.0017$. The inset shows a semi-log plot of $T_{\kappa=\gamma}(\omega/\omega_0)$ of (c) and (f).

However, strong absorption still occurs in the transition region between low-intensity and high-intensity regimes, and the bandwidth of transmitted light in the low-intensity regime is very narrow, significantly limiting the operational range of wavelengths for the protected optical device.

This paper introduces a new limiting scheme based on parity-time (PT) symmetry breaking of reflectionless scattering modes (RSMs) in a passive nonlinear photonic structure with exceptional points of degeneracy (EPDs) (for more details, see Ref. 11). EPDs are spectral singularities associated with non-Hermitian operators, where the eigenvalues and corresponding eigenvectors coalesce. 12–14 Implementing EPDs in the spectrum of an operator can be achieved by imposing PT symmetry. This approach enables a faster-limiting action, thereby reducing photon absorption during the transition from low-intensity to high-intensity states. 11 RSMs are peculiar scattering modes described by steady-state harmonic solutions, where continuous input waves are perfectly impedance-matched, resulting in no back-reflection into the input channels. 15, 16 In the case of negligible absorption, the absence of back-reflection promotes higher transmission. Moreover, at the RSM EPD, the transmission line shape exhibits a flat maximum, creating a passband rather than a narrowband resonance. 16

The proposed OL design features a three-mirror resonator structure composed of alternating layers of cryolite (Na_3AlF_6) and zinc sulfide (ZnS) [Figures 1(a) and 1(d)]. The RSM EPD is achieved by tuning the two coupled cavities of the resonator and the cryolite/ZnS Bragg mirrors. At low intensities, light is transmitted through the structure. However, at intensities exceeding the LT, nonlinear effects are triggered in the ZnS cavity, leading to a detuning of the cavity frequency due to a change in its refractive index. This violates PT symmetry and suppresses RSMs, causing the structure to become highly reflective. 11

The nonlinear effects responsible for the refractive index change can either have a purely optical nature, such as the Kerr effect, with a timescale activation on the order of picoseconds, or a dual nature, such as the thermoptic effect, which operates on timescales of nanoseconds.¹¹ In this numerical and experimental characterization, we focus on the latter.

Another method for achieving optical limiting by disrupting PT symmetry involves changing the angle of incidence, which could help obtain optical isolation at oblique incidence.

2. RESULTS

2.1 Two-cavity OL Design and Modeling

The schematic depiction of a two-cavity OL based on PT-symmetry breaking of RSMs is shown in Figures 1(a) and 1(d). The system consists of two defect states or cavities, one made of cryolite and the other of zinc sulfide, and three Bragg mirrors with alternating layers of these materials. The system can be described by two resonant modes, ω_1 and ω_2 , which are coupled to each other at a rate κ and to the respective external transmission lines at rates γ_1 and γ_2 . The interaction with radiation in this system is described by a 2 × 2 scattering matrix, S, which was evaluated using a coupled mode theory (CMT) approach.¹¹

Considering a continuous wave impinging on the structure from the left, we can define the reflection and transmission coefficients as $r(\omega) \equiv S_{11}(\omega)$ and $t(\omega) \equiv S_{21}(\omega)$, respectively. The specific solutions to the scattering problem where there is no back-reflection into the input channel $(r(\omega_{RZ}) = 0)$, are represented by complex frequencies $\omega_{RZ}^{(1,2)}$, known as R-zeros. These frequencies are found by solving the eigenvalue problem for the non-Hermitian auxiliary wave operator A:

$$\det(\omega_{RZ}\mathbf{I} - \mathbf{A}) = 0, \qquad \mathbf{A} = \begin{pmatrix} \omega_1 & \kappa \\ \kappa & \omega_2 \end{pmatrix} + i \begin{pmatrix} \gamma_1 & 0 \\ 0 & -\gamma_2 \end{pmatrix}, \qquad (1)$$

where I represents the 2×2 identity matrix. When the frequencies are brought onto the real axis, $\omega_{RM}^{(1,2)} = \omega_{RZ}^{(1,2)} \in \mathbb{R}$, their corresponding eigenstates are the reflectionless scattering modes (RSMs).^{15,16} For a passive system (no loss or gain), the RSMs are characterized by unity transmittance, $T\left(\omega_{RM}^{(1,2)}\right) \equiv \left|t\left(\omega_{RM}^{(1,2)}\right)\right|^2 = 1$ [solid green lines in Figure 1(b)]. Through direct diagonalization of A, we can observe that the conditions for the formation of the RSMs are as follows:

$$\omega_1 = \omega_2 = \omega_0, \qquad \gamma_1 = \gamma_2 = \gamma, \qquad \kappa \ge \gamma.$$
 (2)

The first two equations result from imposing PT symmetry on the operator A, such that [A, PT] = 0. The last equation indicates the presence of a *spontaneous* symmetry breaking point, $\kappa = \gamma$, which represents an EPD at $\omega_{EPD} = \omega_0$, where the eigenvalues and eigenvectors coalesce [an open circle in Figure 1(b)].

Around $\omega_{EPD} = \omega_0$ at the RSM EPD, for incident intensities I < LT, the transmission line shape exhibits a quartically flat profile [Figure 1(c)]:

$$T_{\kappa=\gamma}(\omega) = \frac{4\gamma^4}{4\gamma^4 + (\omega - \omega_0)^4}.$$
 (3)

When the incident intensity exceeds the LT (I > LT), the resonant mode in the ZnS cavity is detuned due to the thermo-optic effect, leading to an explicit PT-symmetry breaking. Consequently, the transmission around ω_0 is reduced, and the structure becomes highly reflective. In this case, the RSMs are suppressed, and we can observe real-valued resonance frequencies $\omega_{max}^{(1,2)}$, where the transmittance reaches its maximum [solid green lines in Figure 1(e)]. Around the RSM EPD, the transmittance profile is described by [solid red line plot in Figure 1(f)]:

$$T_{\kappa=\gamma}(\omega) = \frac{4\gamma^4}{4\gamma^4 + \gamma^2 \varepsilon^2 + (\omega - \omega_0)^2 (\omega - \omega_0 - \varepsilon)^2},\tag{4}$$

which exhibits two Lorentzian peaks centered at $\omega_{max}^{(1)} = \omega_0$ and $\omega_{max}^{(2)} = \omega_0 + \varepsilon$.

2.2 Experimental Results

The experimental analysis was carried out on a sample fabricated by Omega Optical LLC (VT, USA). They deposited cryolite/ZnS layers according to the structural scheme shown in Figure 1. This design aimed to create the RSM EPD ($\kappa = \gamma$ in Eq. 2) around ω_0 , which corresponds to a wavelength of $\lambda_0 = 532$ nm. The multilayer was deposited on a Borofloat glass substrate with a diameter of 25.4 mm and a thickness of 0.5 mm. It was then laminated to a glass coverslip using index-matching epoxy (EPO-TEK 301) to resist moisture and mechanical stress

The spectral characterization in the linear regime (low intensity) was performed by oblique-angle transmittance measurements using the experimental setup depicted in Figure 2(a) (see also Ref. 11 for materials and methods). The transmittance spectra measured for s-polarized light are shown in Figure 2(b). At normal incidence, the results show a peak transmittance of 0.75 at 532 nm with a full width at half-maximum (FWHM) of 0.4 nm. As the angle increases, the transmittance drops, indicating PT-symmetry breaking of RSMs. Cavity detuning occurs due to a differential blueshift between the cavities, ¹¹ noticeable from the peak splitting, which becomes more evident as the angle increases [Figure 2(c)]. For example, at an angle of 10° , peak transmittance drops below 0.04, exhibiting a high directional transmission not found in conventional narrow-passband filters. The angular transmission cone of the structure, in terms of FWHM, is $\sim 5^{\circ}$ [inset in Figure 2(b)]. Within experimental error, no difference was found when repeating the measurements using p-polarized light, demonstrating that the system's response is substantially independent of polarization. The directional transmission feature of the system can be utilized in optical isolators to achieve isolation at oblique incidence, lens-free fluorescent imaging, ¹⁷ and for obtaining collimated LED sources. ¹⁸

Optical limiting was explored using the experimental setup schematically depicted in Figure 3(a) (see also Ref. 11 for materials and methods). It consists of a Nd:YAG laser source emitting 532-nm 6-ns laser pulses with a repetition rate adjustable by the operator. The intensity or fluence of the laser pulses reaching the sample was controlled using a series of filters placed in front of it. The transmittance (T) and reflectance (R) values, obtained from single laser pulse measurements, are plotted in Figure 3(b), with blue and red points, respectively, as a function of peak intensity I_p and fluence F. At $F < 10 \text{ mJ/cm}^2$, T has a value of 0.8, while R is slightly below 0.2, regardless of F, indicating low absorptance in the sample and that the system is in the linear regime (blue-shaded region). When the intensity of the laser is raised above the LT, corresponding to $F \ge 10 \text{ mJ/cm}^2$, the optical limiter starts to act: T drops, while R increases, indicating that the system is in the nonlinear regime (white-shaded region). This behavior becomes more pronounced as the fluence increases, reaching $T \approx 0.05$ and $R \approx 0.9$ at $F = 0.7 \text{ J/cm}^2$. As the pulse intensity continues to increase, it reaches a certain value, approximately 10 mg which coincides with the DT, beyond which the sample starts to incur irreversible damage. Indeed,

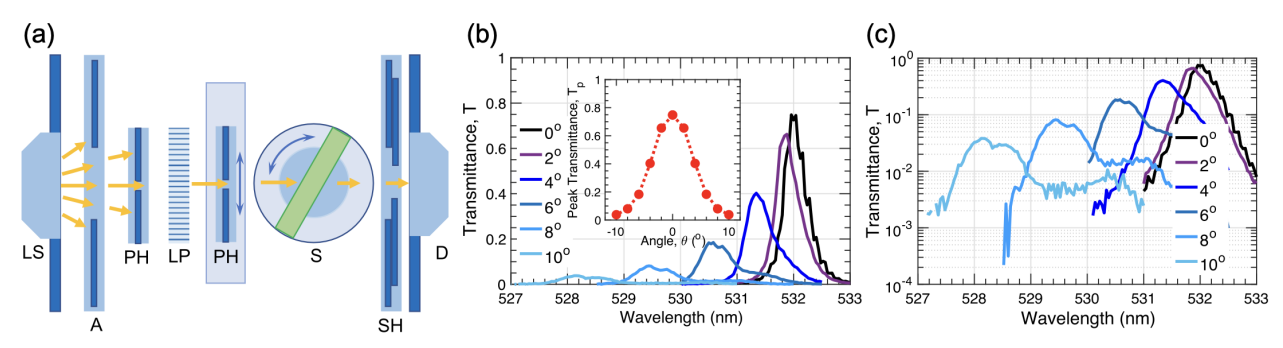


Figure 2. Oblique-angle transmittance measurements of the cryolite/ZnS multilayer: (a), Schematic depiction of the experiment setup showing LS, light source; A, wide aperture; PH, pinholes; LP, linear polarizer; S, sample; SH, shutter; D, detector. (b), Transmittance spectra for s-polarized light as a function of the angle of incidence of the input beam. Inset, angular transmission cone; (c), Semi-logarithmic plot of the transmittance spectra.

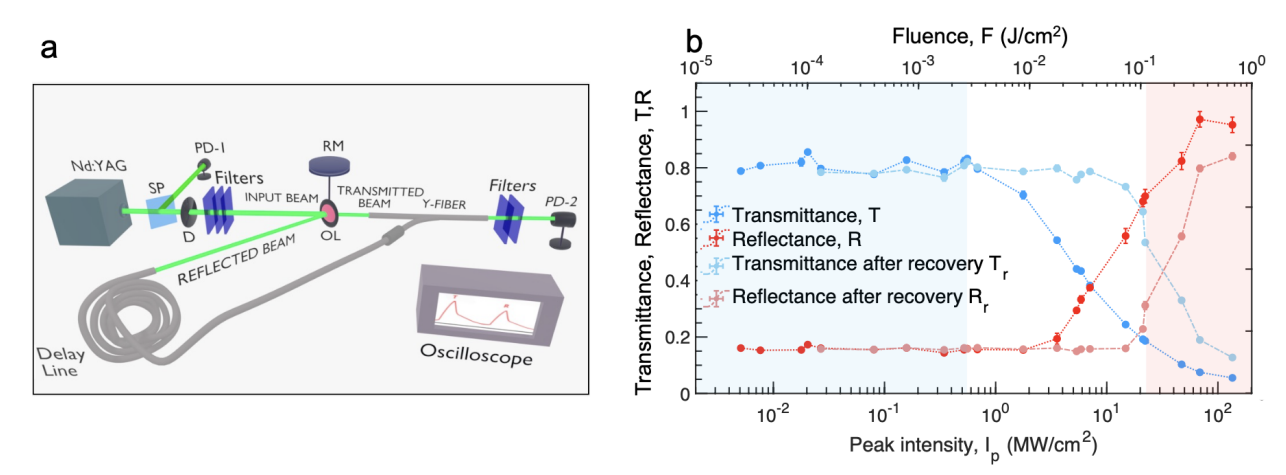


Figure 3. Laser-pulse optical limiting measurements: (a), Schematic depiction of the optical limiting experiment showing the laser pulse source (Nd:YAG). SP, semi-transparent plate; D, diaphragm; RM, rotary translation mount; OL, sample; PD-1, photodiode to measure input energy; PD-2, photodiode to measure the transmitted and reflected energies. (b), $532\,nm$ 6 ns laser pulse transmittance T (blue points) and reflectance R (red points) of the cryolite/ZnS multilayer as a function of the incident peak intensity I_p and fluence F. Also shown are the recovery transmittance T_r (light-blue points) and reflectance R_r (light-red points) measured at the lowest fluence, $25\,\mu J/cm^2$, to monitor the state of the multilayer after each high-fluence measurement. The horizontal parts of the T_r and T_r plots correspond to the full recovery of the multilayer. The blue-shaded, white, and pink-shaded regions indicate the linear, optical limiting, and laser-damage regimes, respectively.

for $F \ge 0.1 \text{ J/cm}^2$, the optical limiting effect is accompanied by structural damage to the system (red-shaded region).

To determine the DT, after each increase in the energy of the incident pulses, the state of the sample was monitored with an additional recovery-check measurement at the lowest fluence $F = 25 \,\mu\text{J/cm}^2$. The "recovery" transmittance T_r and reflectance R_r are plotted along with the corresponding high-fluence measurement data, with light-blue and light-red points, respectively. From these recovery-check points, it is evident that optical limiting is reversible only up to $0.1 \,\text{J/cm}^2$; beyond this value, the structure becomes opaque and ceases to function even at lower intensities in the linear regime. The observed laser-induced damage is attributed to the epoxy layer, as the cryolite and ZnS layers possess a much higher DT.

In our setup, the limiting response is triggered by the thermo-optic effect. PT-symmetry breaking can also be achieved by exploiting the optical Kerr effect; however, higher fluences are required to induce Kerr nonlinearity in cryolite or ZnS cavities.¹¹

2.3 Thermo-Optical Simulations

The experimental results presented in the previous subsection are supplemented with numerical simulations to gain a better understanding of the optical limiting phenomenon induced by the thermo-optic effect. The simulations were performed using COMSOL Multiphysics, considering a 5 ns Gaussian pulse in the setting of Figure 1(a) (see Ref. 11 for further details). The transmittance T and reflectance R were numerically calculated [Figure 4(a)], showing that the system operates in the optical limiting regime within the same fluence range as experimentally observed in Figure 3(b). The analysis was extended to $F = 5 \text{ J/cm}^2$, neglecting the laser-induced damage effect on the multilayer. In Figures 4(b) and 4(c), we show colormaps of the temperature distributions within the system as a function of time for incident pulses with $F = 0.5 \text{ mJ/cm}^2$ (I < LT) and $F = 5 \text{ J/cm}^2$ (I > LT), respectively. Below the LT, the heating of the structure is negligible. However, beyond the LT, the ZnS cavity undergoes significant heating, reaching temperatures of $\sim 200^{\circ}$ C. This temperature is considerably lower than the DT of zinc sulfide, but high enough to trigger the thermo-optic effect and cause a frequency detuning between the cavities. ¹¹

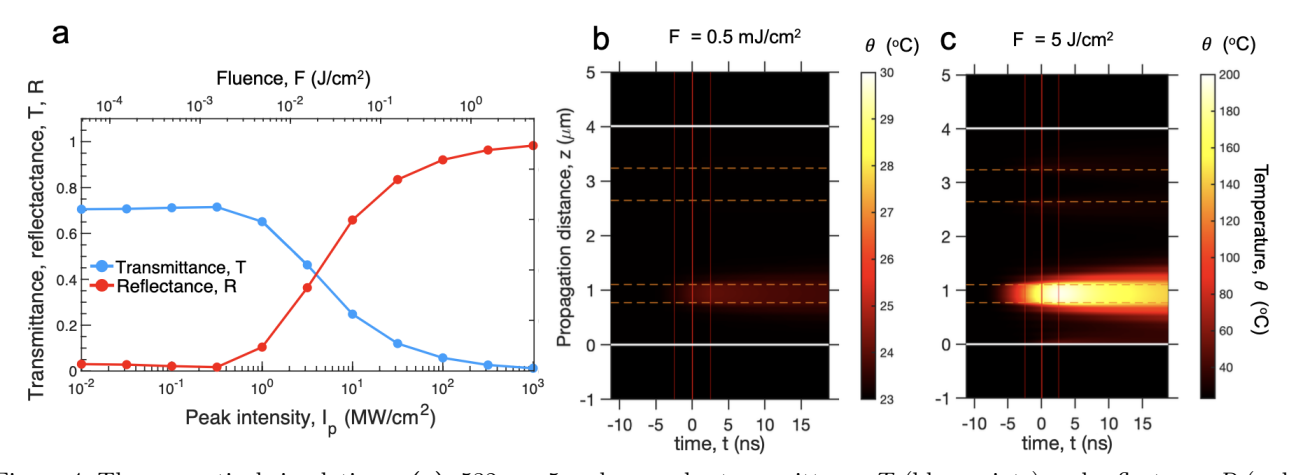


Figure 4. Thermo-optical simulations: (a), 532 nm 5 ns laser pulse transmittance T (blue points) and reflectance R (red points) of the cryolite/ZnS multilayer as a function of the incident peak intensity I_p and fluence F; (b), (c), Temporal temperature profiles across the multilayer for incident pulses of $F = 0.5 \, mJ/cm^2$ (b) and $5 \, J/cm^2$ (c). The upper and lower horizontal dashed lines indicate the cryolite cavity $(Na_3AlF_6)^6$ and the zinc sulfide cavity $(ZnS)^6$, respectively.

Figures 5(a) and 5(b) display the time-resolved transmittance T(t) and reflectance R(t) at the back and

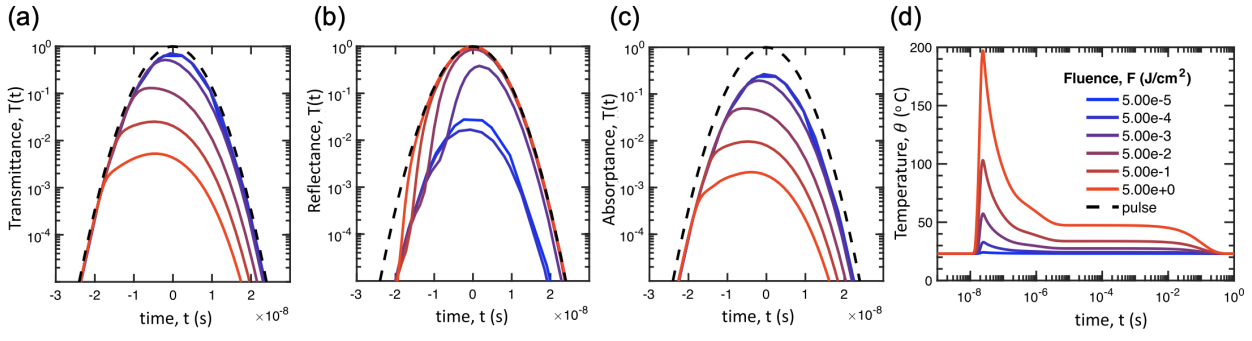


Figure 5. Simulated temporal response of the cryolite/ZnS multilayer under pulsed excitation: (a), Time evolution of the transmitted intensity T(t); (b), Reflected intensity R(t); (c), Absorbed intensity, A(t) = 1 - T(t) - R(t); (d), Temperature $\theta(t)$, following a 5 ns laser pulse excitation for a series of fluences (see figure legend). T(t) and R(t) are measured at the back and front faces of the multilayer, respectively, while $\theta(t)$ is determined in the middle of the zinc sulfide cavity $(ZnS)^6$. The intensity profiles are normalized by the respective incident peak intensities. The black dashed lines are the normalized intensity profile of the incident pulses.

front surfaces of the multilayer, respectively, across various fluence levels. The incident pulse is represented by a dashed line, with each intensity profile being normalized to its peak intensity I_p . The peak intensity I_p intersects the front surface at t=0. For $F\geq 5$ mJ/cm², optical limiting initiates at the leading edge of the incident pulse [Fig. 5(a), negative times] without producing a notable "leakage spike" (i.e., a short-term output power peak). This behavior differs from traditional thermally activated limiting methods, where an extended activation time was seen as a major disadvantage.¹¹

Figure 5(c) depicts the absorptance A(t) = 1 - T(t) - R(t) over time, which decreases consistently with increasing fluence, thereby preventing the optical limiter from overheating. Lastly, Figure 5(d) illustrates the time evolution of the temperature $\theta(t)$ in the center of the zinc sulfide cavity following pulsed excitation. After a rapid temperature increase on the nanosecond time scale, the cavity cools down through a two-stage process. Initially, $\theta(t)$ decreases to a plateau-like state due to heat conductance from the cavity to the surrounding layers of the multilayer. This process takes a few microseconds, with the plateau temperature value being dependent on F. Subsequently, the multilayer cools down to the ambient temperature θ_0 due to heat convection at the front and back surfaces of the multilayer, occurring on a time scale that depends on both F and θ_0 .

3. DISCUSSION

We introduce a new type of passive nonlinear OLs that uses PT-symmetry breaking of RSMs. When the system operates at low fluences or intensities below the threshold, it is in the exact PT-symmetric phase. RSMs create a flat passband around the design wavelength of 532 nm, where an EPD is implemented. However, at high fluences or intensities beyond the LT, the thermo-optic effect induces heating in the nonlinear ZnS cavity, changing its refractive index and subsequent frequency detuning. This detuning explicitly breaks PT symmetry and causes the collapse of RSMs, making the structure highly reflective. The new limiting scheme helps reduce photon absorption during the transition from low to high intensities and forms a passband, which addresses the issue of narrow bandwidths typically seen in single-cavity resonators.

The OL based on the thermo-optic effect is highly scalable and can work across a wide spectral range, from near UV wavelengths to beyond 10 μ m. Moreover, cryolite/ZnS multilayers, a classic film pair used in optical bandpass filters, can integrate optical limiting and filtering functionalities on the same platform across this broad spectral range.

Another way to break PT symmetry is through the purely optical nonlinear Kerr effect; however, we did not observe this effect experimentally during our measurements. PT symmetry can also be disrupted by considering the oblique-angle incidence of light, which we observed in our oblique-angle transmittance measurements in the linear regime. This feature can be beneficial for achieving optical limiting at tilted angles.

Because of our multilayered structure's nonlinear and chiral nature, it displays asymmetric nonlinear transmittance and different limiting thresholds depending on the direction of incidence (see, for example, Ref. 19 and references therein). However, the asymmetry must be sufficiently pronounced in our specific design to be effectively utilized for optical isolation purposes.

4. FURTHER STEPS

To address the issue of excessively narrow spectral bandwidth and increase the passband, a new four-cavity photonic structure made of the same alternating materials (Figure 6) has been designed and produced using a similar deposition technique and lamination process. This passive five-mirror resonator operates at a wavelength of 532 nm. It utilizes the same optical limiting scheme based on PT-symmetry breaking of RSMs as the two-cavity system described earlier. The main difference is that this version is described by a 4×4 Hamiltonian and an associated wave operator \boldsymbol{A} , and it features a higher degree of spatial asymmetry along with a greater number of coupled cavities. Specifically, three of these cavities are filled with the nonlinear material ZnS, while the remaining is cryolite.

One benefit of engineering a resonator with multiple coupled cavities is the widening of the passband.²⁰ Increasing the number of cavities and their coupling strength results in a broader spectral bandwidth around ω_0 at the RSM EPD, as shown in the numerical results in Figure 7. The comparison between the transmittance

spectra of the two-cavity and four-cavity systems is presented here. The FWHM of the spectrum for the four-cavity system (blue line) is approximately 2.4 nm, almost five times wider than the FWHM of the two-cavity system (red line), which is around 0.5 nm.

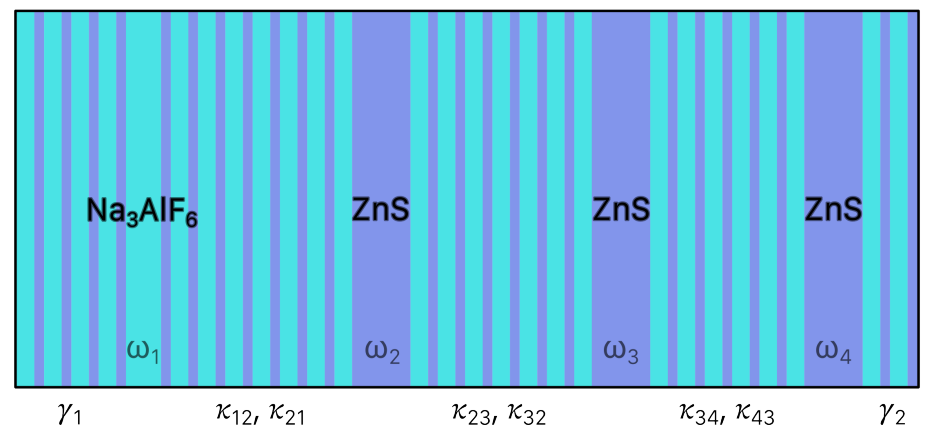


Figure 6. Schematic representation of the four-cavity photonic structure. ω_1 , ω_2 , ω_3 , and ω_4 represent the four resonant modes; κ_{ij} represents the rates related to the coupling between the cavities, while γ_1 and γ_2 represent the rates related to the coupling between the transmission lines and the respective cavities. In *light blue* are the layers made of cryolite (Na_3AlF_6) , and in *purple* are the layers made of zinc sulfide (ZnS).

The transmittance spectra were computed using MEEP (MIT Electromagnetic Equation Propagation). This open-source simulation software uses the finite-difference time-domain (FDTD) method to solve Maxwell's equations within a finite spatial grid.

Another interesting result emerges from analyzing the light transmission through the five-mirror resonator in the linear regime as a function of the incidence angle. To do this, a spectrophotometer was employed, and a roto-translatory mount was carefully assembled to hold and move the sample. Figure 8(a) shows the peak

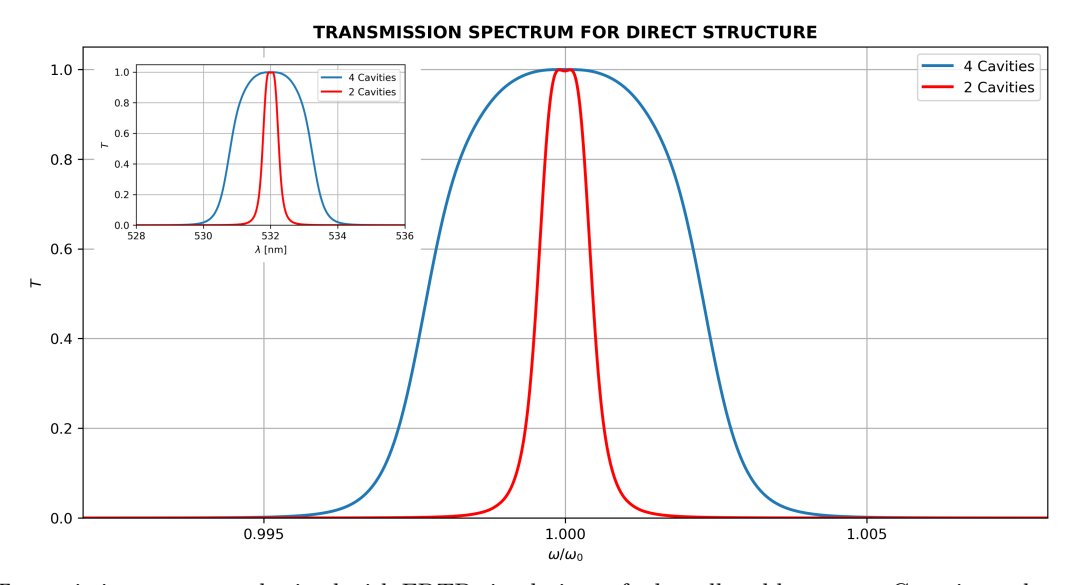


Figure 7. Transmission spectrum obtained with FDTD simulations of a broadband low-power Gaussian pulse propagating through the 4-cavity system (blue) and the 2-cavity system (red). The operational bandwidth of the former is significantly wider compared to the latter, enhancing potential applications. Specifically, the FWHM of the blue peak is approximately $2.4\,nm$, five times wider than the FWHM of the red peak, which is approximately $0.5\,nm$. In the inset, the same spectra are depicted as a function of wavelength λ .

transmittance T_{max} values as red dots, each extracted from a transmittance spectrum at a specific angle versus the incidence angle.

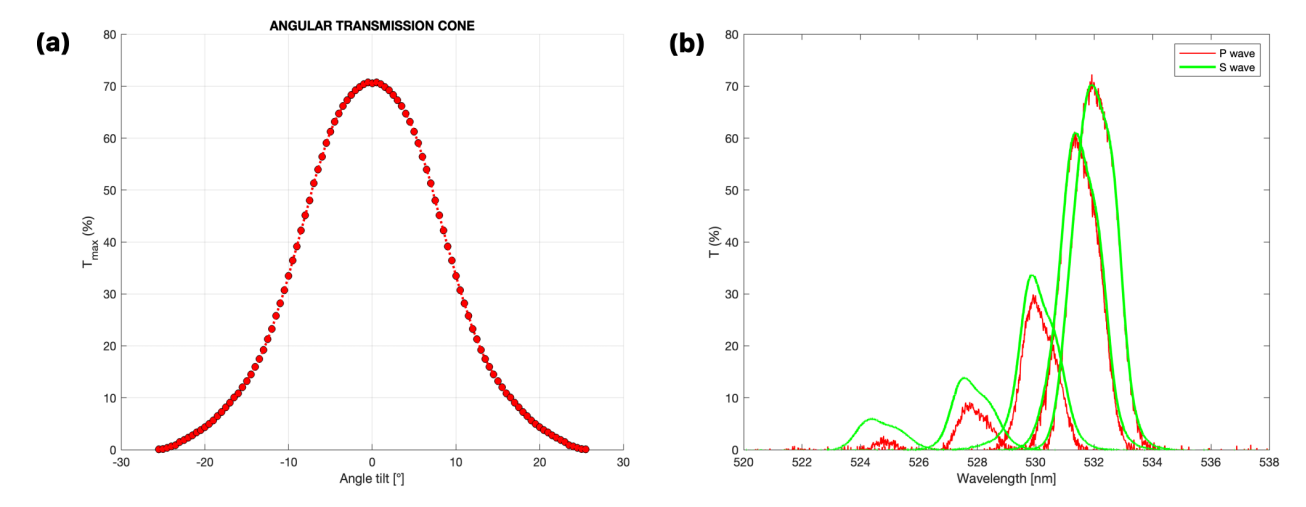


Figure 8. Measurements of transmittance spectra as a function of the incidence angle. (a), The angular transmission cone, which illustrates transmittance peak values as a function of the tilting angle. The transmittance profile is symmetric for positive and negative angles relative to the normal-incidence condition, resulting in a bell-shaped profile. Each red dot in the plot corresponds to a transmittance maximum extracted from a spectrum associated with a specific angle. The FWHM of the angular transmission cone is $\sim 19^{\circ}$. (b), Transmittance spectra retrieved at angles of 0° , 5° , 10° , 15° , and 20° for p-polarized (red lines) and s-polarized (green lines) light. As the tilting angle increases, the p-polarized fields leads to a more rapid decrease in transmittance, coupled with a more pronounced narrowing of the spectra.

In the four-cavity system, the FWHM of the angular transmission cone is $\sim 19^{\circ}$, which is much broader than that of the two-cavity system, which is about 5° . Examples of transmittance spectra at various angles of incidence are shown in Figure 8(b) for both p-wave (red) and s-wave (green) polarizations. The spectra are displayed for normal incidence, 5° , 10° , 15° , and 20° . The experimental bandwidth at normal incidence aligns with the numerical result in Figure 7. Light incidence at an oblique angle causes a differential blueshift between the four cavities. This can be seen in the deformation of the spectra and how the peaks split, although we couldn't fully see this due to low resolution. At higher angles, the bandwidth narrows a bit, and there is a decrease in the amount of light that passes through. For instance, at an incidence angle of approximately 20° , the peak transmittance decreases to 0.04, which was previously seen at around 10° in the two-cavity system. Up to $\sim 5^{\circ}$, this behavior is the same no matter the polarization of the light. But as the angle increases, the spectra seen for the two polarizations start to differ, and this becomes more noticeable at higher angles. In particular, the effects of tilting on the light passing through are slightly stronger when the system is exposed to p-wave radiation.

ACKNOWLEDGMENTS

FR, DW, AB, FT, and SC thank Lorenzo Fini and Renato Torre for lab equipment and helpful suggestions. AAC acknowledges the hospitality of the European Laboratory for Nonlinear Spectroscopy during his sabbatical visit. LS thanks Alice Boschetti and Lorenzo Pattelli for their valuable support with the spectrophotometer operations and the numerical codes.

Research funded by: Air Force Office of Scientific Research (AFOSR) (FA9550- 20-F-0005, FA9550-22-1-0290, LRIR 21RYCOR019); Office of Naval Research (ONR) (N00014-191-2480); National Science Foundation (NSF) (ECCS2148318); Simons Foundation (MPS-733698); Programma Operativo Nazionale Ricerca e Competitività (MD.1062/2021); Ente Cassa di Risparmio di Firenze.

REFERENCES

- [1] Wood, G. L., Clark, W. W., Miller, M. J., Salamo, G. J., and Sharp, E. J., "Evaluation of passive optical limiters and switches," *Proc. SPIE* 1105, 154–180 (1985).
- [2] Scalora, M., Dowling, J. P., Bowden, C. M., and Bloemer, M. J., "Optical limiting and switching of ultrashort pulses in nonlinear photonic band gap materials," *Phys. Rev. Lett.* **73**, 1368–1371 (1994).
- [3] Kahn, L. M., "Optical power limiting in multilayer systems with nonlinear response," *Phys. Rev. B* 53, 1429–1437 (1996).
- [4] Tran, P., "Optical limiting and switching of short pulses by use of a nonlinear photonic bandgap structure with a defect," J. Opt. Soc. Am. B 14, 2589–2595 (1997).
- [5] Ma, G., Shen, J., Zhang, Z., Hua, Z., and Tang, S. H., "Ultrafast all-optical switching in one-dimensional photonic crystal with two defects," Opt. Express 14, 858–865 (2006).
- [6] Kuhl, U., Mortessagne, F., Makri, E., Vitebskiy, I., and Kottos, T., "Waveguide photonic limiters based on topologically protected resonant modes," *Phys. Rev. B* 95, 121409 (2017).
- [7] Reisner, M., Jeon, D. H., Schindler, C., Schomerus, H., Mortessagne, F., Kuhl, U., and Kottos, T., "Self-shielded topological receiver protectors," *Phys. Rev. Appl.* **13**, 034067 (2020).
- [8] Makri, E., Ramezani, H., Kottos, T., and Vitebskiy, I., "Concept of a reflective power limiter based on nonlinear localized modes," *Phys. Rev. A* 89, 031802 (2014).
- [9] Makri, E., Kottos, T., and Vitebskiy, I., "Reflective optical limiter based on resonant transmission," Phys. Rev. A 91, 043838 (2015).
- [10] Vella, J. H., Goldsmith, J. H., Browning, A. T., Limberopoulos, N. I., Vitebskiy, I., Makri, E., and Kottos, T., "Experimental realization of a reflective optical limiter," *Phys. Rev. Appl.* 5, 064010 (2016).
- [11] Riboli, F., Kononchuk, R., Tommasi, F., Boschetti, A., Suwunnarat, S., Anisimov, I., Vitebskiy, I., Wiersma, D. S., Cavalieri, S., Kottos, T., and Chabanov, A. A., "Optical limiter based on pt-symmetry breaking of reflectionless modes," Optica 10, 1302–1309 (2023).
- [12] Ş. K. Ozdemir, Rotter, S., Nori, F., and Yang, L., "Parity-time symmetry and exceptional points in photonics," *Nat. Mater.* **18**, 783–798 (2019).
- [13] Miri, M. A. and Alù, A., "Exceptional points in optics and photonics," Science 363, 1–11 (2019).
- [14] El-Ganainy, R., Makris, K. G., Khajavikhan, M., Musslimani, Z. H., Rotter, S., and Christodoulides, D. N., "Non-hermitian physics and pt symmetry," *Nat. Phys.* **14**, 11–19 (2018).
- [15] Sweeney, W. R., Hsu, C. W., and Stone, A. D., "Theory of reflectionless scattering modes," Phys. Rev. A 102, 063511 (2020).
- [16] Stone, A. D., Sweeney, W. R., Hsu, C. W., Wisal, K., and Wang, Z., "Reflectionless excitation of arbitrary photonic structures: a general theory," *Nanophotonics* **10**, 343–360 (2021).
- [17] Sasagawa, K., Kimura, A., Haruta, M., Noda, T., Tokuda, T., and Ohta, J., "Highly sensitive lens-free fluorescence imaging device enabled by a complementary combination of interference and absorption filters," *Biomed. Opt. Express* 9, 4329–4344 (2018).
- [18] Vázquez-Moliní, D., González-Montes, M., Álvarez, A., and Bernabéu, E., "High-efficiency light-emitting diode collimator," Opt. Eng. 49, 123001 (2010).
- [19] Chenghao, W., Horak, E. H., King, J., Salman, J., Zhang, Z., Zhou, Y., Roney, P., Gundlach, B., Ramanathan, S., Goldsmith, R. H., and Kats, M. A., "Limiting optical diodes enabled by the phase transition of vanadium dioxide," ACS Photonics 5, 2688–2692 (2018).
- [20] Sounas, D. L., Soric, J., and Alù, A., "Broadband passive isolators based on coupled nonlinear resonances," Nat. Electron. 1, 113–119 (2018).